Comparison of Multi-Parallel Slit and Knife-Edge Slit Prompt Gamma Cameras in the context of hadrontherapy verification

Brent F. B. Huisman[1,2], É. Testa[2], and D. Sarrut[1]

[1] CREATIS, Université de Lyon; CNRS UMR5220; INSERM U1206; INSA-Lyon; Université Lyon 1; Centre Léon Bérard, Lyon, France
[2] IPNL, Université de Lyon; CNRS/IN2P3 UMR5822; Université Lyon 1 Lyon, France
E-mail: brent.huisman@cern.ch

April 18, 2019

Abstract

Purpose:
Materials and Methods:
Results:
Conclusion:

Contents

1 Introduction

The well-defined range of particles in matter is the main reason they are used in cancer treatment today. Unfortunately we are not able to take full advantage of this property, because of uncertainties in patient positioning, the proton range, patient anatomy, and the Hounsfield unit to particle stopping power conversion (Paganetti, 2012). Often, medical practice is to plan conservatively, namely adding margins around the tumor, greatly reducing the potential benefits of particle treatment (Knopf and Lomax, 2013). Online monitoring would make measurements of uncertainties such as mentioned above possible, and thereby permit more precise planning which could take maximum advantage of the steep BP fall-off and reduce damage to tissues surrounding the tumor. A new way to perform monitoring is to use prompt gammas (PGs), a natural byproduct in particle treatments and are of prime interest (Golnik et al., 2014; Gueth et al., 2013; Janssen et al., 2014; Moteabbed et al., 2011). A knife-edge PG camera (Perali et al., 2014; Richter et al., 2016) was put into clinical operation in fall 2015, at OncoRay in Dresden, Germany. The aim of such collimated cameras is to obtain a 1D profile of the PG production along the beam direction and obtain the position of the fall-off of the signal, which is strongly correlated to the BP position. Other approaches include detection of the target materials using a spectral PG camera (Verburg and Seco, 2014), using the primary particle's time of flight (ToF) in a timed PG measurement (Golnik et al., 2014) and Compton camera designs (Kurosawa et al., 2012; Llosá et al., 2016; Polf et al., 2015; Roellinghoff et al., 2011; Solevi et al., 2016; Thirolf et al., 2016).

To date two publications have attempted to perform an in-depth comparison between two collimated PG camera designs. Smeets et al. (2016) showed an experimental comparison of the knife-edge camera with a non-optimized CLaRyS MPS camera (some technical constraints prevented the authors to use the "optimal CLaRyS design". In Lin et al. (2017) a MC comparison is executed on their own two collimator designs. Although the aforementioned studies may give the impression to provide a fair comparison (use of the same absorbers, same beam-collimator and collimator-absorber distance in the case of Lin et al. (2017)), they do not provide a thorough justification of their sets of parameters. Surprisingly, some parameters are even not the same between the two camera types. While it can be understood in Smeets et al. (2016) due to experimental constraints, it is more questionable in Lin et al. (2017) (different energy deposition selection).

While very interesting, such comparisons could be supported by more theoretical considerations on the expected output and camera parameters. Taking a step back, the 1D PG signal can be paramatrized, as well as the relevant dimensions of the PG collimator, the event selection criteria. A simple model could be built relating these factors which in turn can be tested in a study.

This publication will demonstrate and validate a model for a knife-edge slit (KES) and multiparallel slit (MPS) collimator designs, both analytically and by using Monte Carlo (MC) studies. The objectives of the present paper are the following:

- Develop an analytical model based on geometric considerations

  - The model should allow for a theoretical estimation of the detection efficiency and spatial resolution, for both MPS and KES and so allow for conclusions to be drawn about the intrinsic features of MPS and KES collimators.

  - Validate the analytical model using MC studies.

  - Address deficiencies in previous studies. In Smeets et al. (2016) and Lin et al. (2017): the KES/MPS detection efficiency ratio is 1.6 for Smeets 2016 and 5.3 for Lin 2017, assuming the use of the same energy window. These comparisons were not performed under identical conditions, nor were differences accounted for.

- Prototype comparison

  - The clinically relevant parameter is, currently, the fall-off position (FOP), allowing for a BP verification. The prototypes will thus be compared on that merit.

was it the same energy window?

I think so. Certainly for Smeets 2016

2 Materials and Methods

2.1 Analytical model for spatial resolution and detection efficiency

Camera performance is mainly characterized by a compromise between spatial resolution and detection efficiency. During camera design, modifications of some geometrical parameters, such as collimator-crystal distance, collimator pitch or depth..., often lead to improvement of one of this criteria and deterioration of the other. In order to compare performance of different camera types and configurations, we derive an analytical model that predict camera performance for both Multi Parallel Slit (MPS) and Knife Edge Slit (KES) collimators. Such models allow to estimate variation in performance according to variation in geometrical parameters assuming that the camera absorber allows for a perfect gamma detection (full absorption on absorber entrance surface). The models will be evaluated against Monte-Carlo simulations in next sections.

The figure **??** first defines several generic geometrical parameters, namely: d_1 the source to MPS-collimator distance, d_2 the MPS-collimator to crystal distance, D the MPS-collimator depth, d_1' the source to KES-collimator center distance, d_2' the KES-collimator center to crystal distance, $L_{MPS} = d_1 + D + d_2$ or $L_{KES} = d_1' + d_2'$ the total source-crystal distance, H the camera height, p the MPS collimator pitch, f the fill factor (ratio between septa width and the pitch), s the slit width and α the KES-collimator angle. All distance values are in millimeters.

I would replace this paragraph by the following table

	MPS	KES
Source-collimator distance	d_1	d_1'
Collimator-absorber distance	d_2	d_2'
Source-absorber distance	$L = d1_D + d_2$	$L = d_1' + d_2'$
Collimator thickness	D	T
Knife-edge slit angle	$\varnothing$	α
Slit width		s

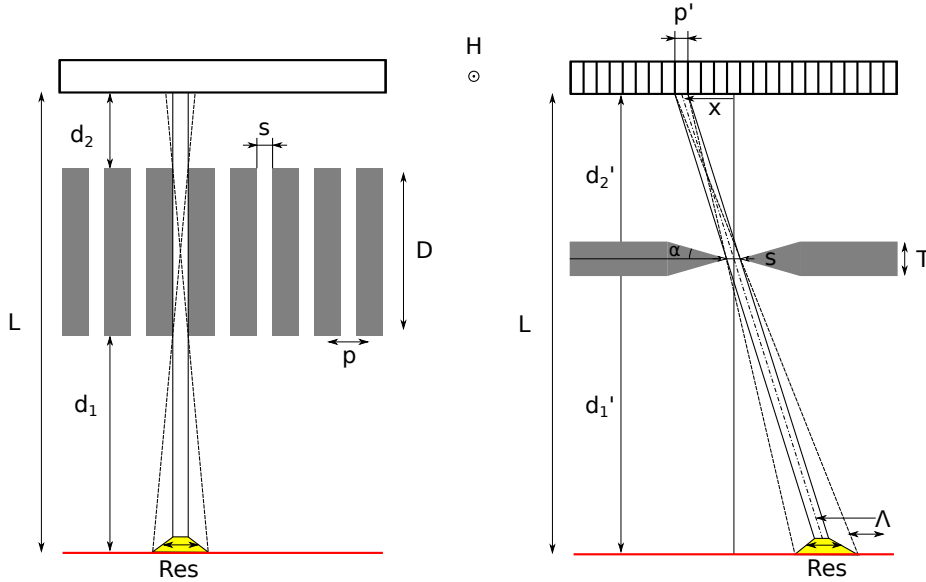Table 1: Geometrical parameters of the MPS and KES cameras.

Figure 1: Schemes of MPS and KES cameras.

2.1.1 Spatial resolution

From a geometrical point of view, the spatial resolution is characterized by the *detector unit field of view*, denoted Res . This is the portion of the source that can be seen through a single camera unit: a single slit for the MPS and a single detector unit for KES. The probability of a photon emitted at a given point along a linear source perpendicular to the slit plane to reach this detector unit can be described as an isosceles trapezoid whose width of the top segment corresponding to the slit width while the width of the base segment is equal to the sum of the slit width and the penumbra. We defined Res as the FWHM of this trapezoid, see eq 1 and 2.

$$\text{Res}^{\text{MPS}} = s\left(1 + \frac{d_1}{D}\right) = p(1-f)\frac{D+d_1}{D} \tag{1}$$

$$\text{Res}^{\text{KES}} = s\left(1 + \frac{d_1'}{d_2'}\right) = \frac{sL}{d_2'} \tag{2}$$

If collimator transparency is neglected, Res is fully defined by geometrical parameters, in particular the slit width s. However, prompt gamma have high penetration capability that can not be neglected in the case of KES where the collimator depth is very small in the region of the knife edge around the slit. Indeed, we define the *Effective Slit Opening* s_e that can be used in the evaluation of the field of view and the efficiency in place of the geometrical slit width. Metzler et al. Metzler and Accorsi (2005) proposed a method to estimate the effective slit width, specifically to calculate the spatial resolution accurately. The proposed expressions were based on one-dimensional cuts through the pinhole geometry and can be applied directly to a knife-edge geometry without modification. Their approach is for a point source and dependent on the location of the source within the Res . For a source in the center, it simplifies to eq. 3 with μ the linear attenuation length of the radiation in the collimator material.

$$s_e = s + \frac{\ln 2}{\mu \tan \alpha} \tag{3}$$

$$\text{Res}^{\text{KES}} = s_e\left(1 + \frac{d_1'}{d_2'}\right) = \frac{s_e L}{d_2'} \tag{4}$$

Hence, eq. 1 and eq. 4 represent the spatial resolution of the two KES and MPS camera systems according to simple geometrical and gamma attenuation parameters (collimator distances, angle and collimator linear attenuation length). The spatial resolution is expressed in millimeters.

2.1.2 Detection efficiency

The probability that a photon emitted from a point facing a slit to reach the detector is described by the solid angle Ω_D from that point to the detector. For MPS, the solid angle is composed of the azimuthal angle β and the polar angle. With small angle approximation, it is described by eq.5. Note that this is true only when the Ω_D is limited by the slit width, i.e. the crystal sizes and distances are such that all photons that cross the collimator impinge on detector material. For KES, the solid angle under which a point of the source sees a crystal of the detector depends on the location of the point source, x, since the distance between source and crystal changes significantly over the field of view of the camera. We consider the solid angle for a point of the source that is within the central part of the field of view of the crystal at location x on the detector plane (the origin of the detector plane facing the center of the slit). Under small angle approximation, the solid angle is given eq. 6.

$$\Omega_D^{\text{MPS}} = \frac{H}{L}\beta = \frac{H}{L}\frac{s}{D+d_1} \tag{5}$$

$$\Omega_D^{\text{KES}} \quad = \quad \frac{wHL}{\Lambda^3(x)} = \frac{Hp}{L^2\left(1 + \frac{x^2}{d_2'^2}\right)^{3/2}} \tag{6}$$

with Λ the distance between the source point and the crystal in the KES.

We consider that a detection unit correspond to a single detector. The corresponding detection efficiency, denoted Eff, can be expressed as: $\text{Eff} = \text{GDE} \times f_{\text{FOV}}$, with GDE the geometrical detection efficiency with the solid angle of a point that sees a detector through the slit, and $f_{\text{FOV}} = \frac{\text{Res}}{p}$ the FOV factor where p is the pitch of the camera (in practice the width of the detector unit). This FOV factor corresponds to the fraction of the source seen by the camera. It is in principle larger than 1 since cameras are usually designed to see all the source without any hidden regions. The detection efficiency per detector unit is then given by eq. 7 and 8.

$$
\begin{aligned}
\text{Eff}^{\text{MPS}} \quad &= \quad \frac{\Omega_D^{\text{MPS}}}{4\pi} \frac{\text{Res}^{\text{MPS}}}{p} \\
&= \quad \frac{1}{4\pi} \frac{H}{L} \frac{s}{D + d_1} p(1 - f) \frac{D + d_1}{D} \frac{1}{p} \\
&= \quad \frac{Hs(1-f)^2}{4\pi LD}
\end{aligned}
\tag{7}
$$

$$
\begin{aligned}
\text{Eff}^{\text{KES}} \quad &= \quad \frac{\Omega_D^{\text{KES}}}{4\pi} \frac{\text{Res}^{\text{KES}}}{p} \\
&= \quad \frac{s_e H}{4\pi d_2' L} \frac{1}{\left(1 + \frac{x^2}{d_2'^2}\right)^{3/2}}
\end{aligned}
\tag{8}
$$

The formulas of detection efficiency and spatial resolution of MPS and KES cameras are gathered in table 2. The most striking feature of theses formulas is their similarities. Indeed if we consider perfect collimators with infinite absorption capacity then the effective slit width of the KES (s_e) is equal to s and the filling factor f of the MPS can be decreased down to zero. In such conditions,

	MPS	KES
Effective slit width (s_e)	s	$s + \frac{\ln(2)}{\mu \tan(\alpha)}$
Spatial resolution (Res)	$s\left(1 + \frac{d_1}{D}\right)$	$s_e\left(1 + \frac{d_1'}{d_2'}\right)$
Detection efficiency (Eff)	$\frac{Hs}{4\pi LD}(1-f)$	$\frac{Hs_e}{4\pi Ld_2'}\left(1 + \frac{x^2}{d_2'^2}\right)^{-3/2}$
Collimator effective thickness (T_e)	$D \times f$	T

Table 2: MPS and KES detection efficiencies and spatial resolutions from the analytical model. The parameters of the cameras are defined in figure 1.

2.2 Monte Carlo simulations

- Analytical model verification (AMV): Fair comparison of the two types of collimators with MC simulations. What does it mean?

  - Use of same absorbers (the LYSO absorber of the KES prototype that we can consider as the reference), the same energy selection which was not the case in Lin 2017 and the same TOF selection (no TOF)

  - Then a discussion of the results in the light of the analytical models

- Note: the KES background level can be obtained from Figure 18 in Perali 2014. Regarding the MPS background level I propose to use the same level as the one of KES for the following reasons: i) the background level in the MPS camera is derived in Pinto 2014 from measurements with large detectors by assuming that the background is proportional to the detector volume. If we apply the same approach, it is reasonable to use the same background levels since we use the same absorbers for MPS and KES. One can argue that the MPS and KES collimators are different. It is true and it is difficult to say whether the larger amount of material in the CLaRyS MPS collimator leads to a larger background with more neutron-induced gammas or a lower background due to a larger attenuation of these gammas... At first order the background levels should be similar and a first order estimate is sufficient for a paper that mainly aims at comparing the signal detection of the two cameras.

- Simulations of the two prototypes as they are published (results of the submitted paper with the "regular" cylindrical PMMA target of 15 cm diameter and 20 cm lenght).

  - ⇒ Comparison of the two prototypes
  - Note that the absorbers have different thicknesses

2.2.1 Simulation tool

Imaging paradigms such as PG detection are evaluated against experiments, and often also with Monte Carlo (MC) simulations (Golnik et al., 2014; Gueth et al., 2013; Janssen et al., 2014; Moteabbed et al., 2011; Robert et al., 2013). For rarely occurring processes such as PG simulation, convergence to the model of the truth to within acceptable statistical error can be slow. This paper presents an *in silico* study of the feasibility of the clinical relevance of PG FOP estimation using collimated cameras, and uses the vpgTLE variance reduction method described in Huisman et al. (2016). vpgTLE is a two stage process, where firstly a PG yield distribution image is estimated, which in the second stage is used as a PG source with which detectors can be investigated. Gate 7.2 (Sarrut et al., 2014) with Geant 4.10.02 and the QGSP_BIC_HP_EMY physics list, commonly used for PG studies, are used in this analysis. Thanks to vpgTLE, simulations for about 10^9 protons (about 6×10^8 photons) took 1-2 hours on a single core of an Intel(R) Core(TM) i7-3740QM.

2.2.2 PG Camera modeling

Two PG detectors tailored to FOP verification (illustrated in fig. 2) were chosen:

- the CLaRyS multi-parallel-slit (MPS) camera, Case 1 (Pinto et al., 2014)
  This camera intends to measure the whole PG profile to control ion-ranges in the patient with a field of view (FoV) of 300 mm. It consists of a bismuth germanium oxide (BGO) absorber and a tungsten alloy collimator. It makes use of ToF selection to reduce the neutron background. In the optimization carried out by Pinto et al. (2014), parameters such as collimator pitch, axis-to-collimator and axis-to-detector were varied, and their impacts evaluated in terms of fall-off retrieval precision (FRP) and spatial resolution (sharpness of the fall-off region). Here, configuration 1 (with relaxed constraints on spatial resolution) was chosen for its optimal FRP performance. As was done by Pinto et al. (2014), the camera lengths (collimator and scintillator volume) are chosen *up to* 300 mm, such that the length is an integer multiple of the pitch size, with for the collimator a collimator-leaf-width extra, to ensure each pixel has a leaf on both sides. With the 8 mm pitch and 2.6 mm collimator-leafs, this results in a scintillator volume of length 296 mm and collimator length 298.6 mm.

  Check the material used in "Prototypes comparison". Did you use BGO for MPS?

- the IBA knife-edge (KES) camera (Perali et al., 2014; Sterpin et al., 2015)
  The purpose of this camera consists of verifying the BP position with a FoV of 100 mm. It consists of a Cerium doped Lutetium based (LYSO) absorber and a tungsten alloy collimator. Richter et al. (2016) provides the first clinically obtained results. At this time, no other camera has been subjected to clinical tests, which is why we consider this prototype a benchmark.

Regarding background ToF selection, for the IBA C230 accelerator with a period of 10 ns, Pinto et al. (2014) chose a window of 4 ns around the PG maximum, based on experimental ToF spectra. This means that about 60% of the noise could be removed. For the KES prototype ToF is not used,
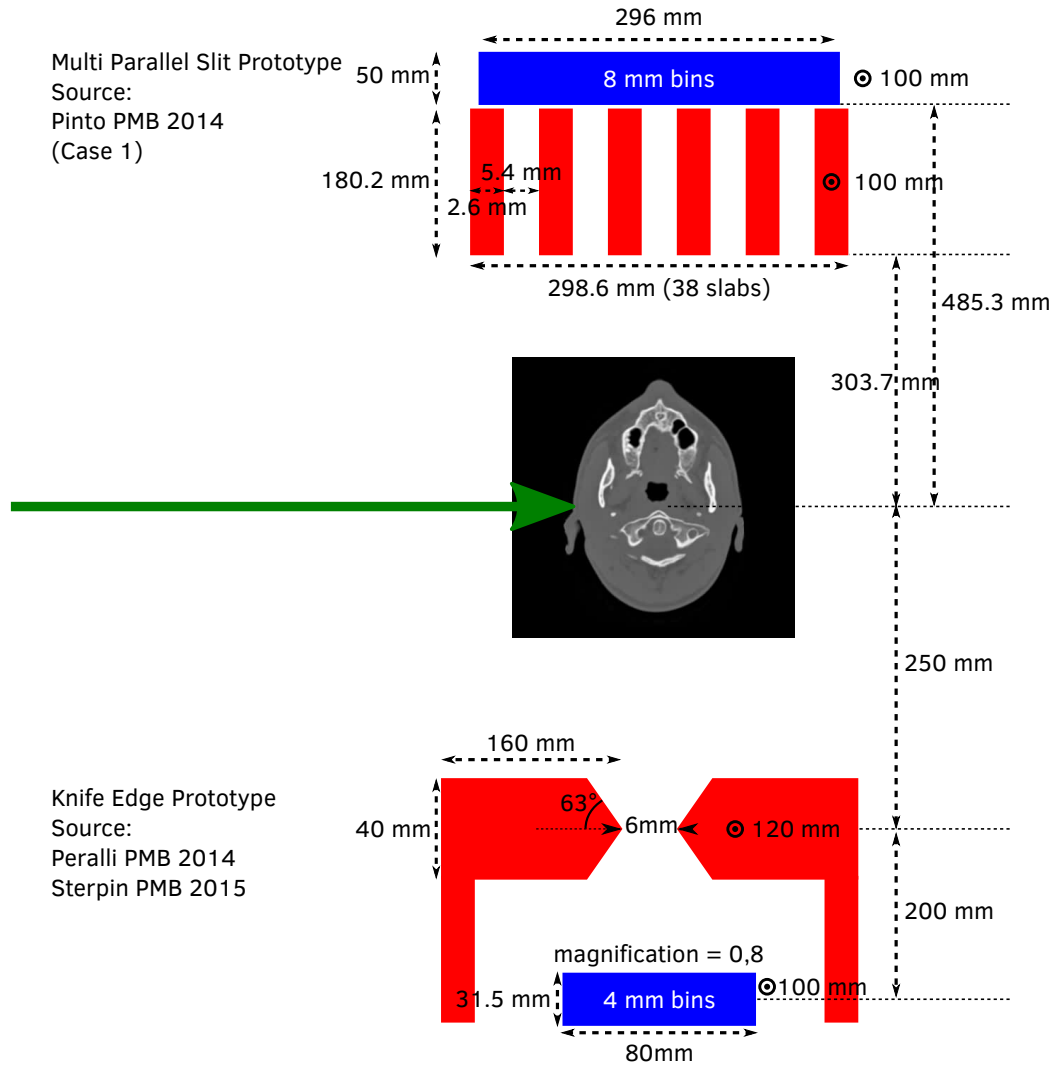
Figure 2: Schematic presentation of the two PG cameras considered in this study. The green arrow represents the proton beam. In red the collimation elements and in blue detection elements. The dimensions were taken from Pinto et al. (2014) and Perali et al. (2014); Sterpin et al. (2015). Note that the two cameras have an identical detector height (⊙ symbol), the two cameras were positioned at an identical location above the head during all simulations, and that here they are not drawn to scale.

leading to a higher background, as is evident when one compares the backgrounds as published in the two publications. A second difference is the energy selection window. The IBA group employ a 3-6 MeV window, whereas the CLaRyS collaboration produced their optimization with a 1-8 MeV window. We will compare each camera with their published properties, that is to say: a 1-8 MeV window and ToF for MPS and a 3-6 MeV window without ToF for KES.

Both PG camera prototypes have different photodetectors and different detector electronics. In this study, these differences are not implemented. Instead, the method as described in Gueth et al. (2013) was used to obtain the interaction point of an impinging photon. If the integrated energy deposited in a crystal lies in the acceptable energy and ToF window, the event is recorded. The position of the event in the crystal is considered as the energy weighed barycenter of all interactions in the crystal, plus a random value taken from a 5mm FWHM Gaussian to simulate the electronics and the detector resolution.

2.2.3 Background modeling

Background estimation in PG simulation is a difficult and largely unsolved issue (Huisman et al., 2016; Perali et al., 2014; Pinto et al., 2014; Sterpin et al., 2015). Simulations would ideally include beam nozzle and whole room modeling, but these are habitually omitted. ToF selection techniques can improve the signal-to-noise ratio (SNR) (Roellinghoff et al., 2014; Testa et al., 2008), but then depend on the proper simulation of the beam accelerator time structure. As noted in Huisman et al. (2016), no validation for background in PG simulations has been performed at this time. In this study, the stable time structure of current generation cyclotrons was assumed, in which the neutron background is largely constant.

Estimates of background counts in the detector are taken from Perali et al. (2014); Pinto et al. (2014), which are both based on measured data:

- MPS: Pinto et al. (2014) fig. 9: $1 \cdot 10^3 \pm 1 \cdot 10^2$ per $4 \cdot 10^9$ primary protons per 8 mm bin
  Converted to per primary proton: $2.5 \cdot 10^{-7} \pm 0.25 \cdot 10^{-7}$
- KES: Perali et al. (2014) fig. 11: $5 \cdot 10^{-7} \pm 0.5 \cdot 10^{-7}$ per primary proton per 4 mm bin

Per unit of bin length, the background yield of the MPS with ToF is therefore 4 times as low as the background seen with the KES. In the context of the fair comparison, for the KES camera the background with ToF can be obtained by multiplying the background with the same $\frac{4ns}{10ns} = 0.4$ fraction as with the MPS.

2.2.4 Beam and target

We use the test-case presented in Perali et al. (2014) as the KES detector properties such as background were published for that scenario, again in order to remove any doubt that a difference in camera performance could be due to a difference in implementation or setup. A 160 MeV mono-energetic proton beam is shot into a cylindrical PMMA phantom (length 30 cm, radius 15 cm). Employing the batch method we realize 50 simulations for each experiment.

2.2.5 AMV-specific alterations to setup

In the case of simulation for analytical model verifications, we use identical absorbers for both prototypes, namely the absorber of the KES prototype and we apply the same energy and TOF selection: the same energy selection ($E > 1$ MeV) and the same TOF selection (no TOF selection). Since AMV deals with gamma detection, no background modeling is applied in this AMV-specific setup.

Table 3 gives an overview of the main cameras parameters used for AMV and prototypes comparison.

2.3 Figures of merit

2.3.1 Analytical Model Verification

The comparison of the analytical model with Monte Carlo simulations will performed on the two features predicted by the model, namely the detection efficiency and the spatial resolution

		Analytical model verification	Prototypes comparison
Absorber	MPS	LYSO	BGO
	KES		LYSO
Energy selection	MPS	>1 MeV	>1 MeV
	KES		3–6 MeV
TOF selection	MPS	no TOF	TOF
	KES		no TOF
Background modeling		No modeling	Experimental data based modeling

Table 3: Summary of the main cameras parameters used for AMV and prototypes comparison.

Detection efficiency   We can compare the detection efficiency of camera unit with two MC estimates:

- the detection efficiency of a camera unit defined as the ratio of the mean number of detected gammas over the number of emitted gammas for camera units seeing the PG profile,

- the PG falloff contrast (FOC), which we define as the difference between peak and background, normalized by the number of primaries and per millimeter (since the two cameras have differing bin sizes).

The two quantities are strongly correlated. The former directly corresponds to the definition of the anaytical detection efficiency DE_{cu} the latter accouts for the partial collimator transparency and it is the camera endpoint in the context of ion-range verification.

we must mention which background we use here.

Spatial resolution   Let us define the width of the PG profile fall-off (FOW) as the FWHM of the peak resulting from the computation of the PG profile first derivative.

The FOW of the detected PG profiles can be obtained in principle using summation in quadrature of the FOW of PG emission profiles (FOW_{e}) and the spatial resolution of the cameras (Res). Since $FOW_{e} \sim 5$ mm according to simulated profiles (Krimmer et al., 2017) and Res of the MPS and KES prototypes ranges from 10 to 20 mm (Pinto et al., 2014; Smeets et al., 2012), we can consider that FOW is mainly determined by the camera spatial resolution (Res).

2.3.2   Prototype Comparison

In the comparison of the nominal (unequalized) prototypes, we also take a look at the figures of merit (summarized in table 4). In addition, because of its clinical relevance, the fall-off retrieval precision (FRP) will be determined. The FRP is the standard deviation of the FOP, which is obtained by way of the batch method. Each of these can then be examined as function of the energy and ToF selections.

Table 4 presents the figures of merit used for the analytical model verification and the prototypes comparison.

	Analytical	MC	
Detection efficiency	Eff	Eff$_{MC}$	FOC
Spatial resolution	Res	FOW	

Table 4: Figures of merit for the analytical model verification. Eff$_{MC}$ refers to the *signal* (PG) detection efficiency. FOC: Fall-off contrast. FOW: Fall-off width.

3   Results

3.1   Analytical Model Verification

The FOW shown in table 5 shows that both cameras perform similar with ToF selection. For the MPS the ToF selection makes no difference (up to 2%), while for the KES it gives a 10-20% improvement.

Time selection	ToF				none			
Energy selection	1		3		1		3	
Camera	MPS	KES	MPS	KES	MPS	KES	MPS	KES
FOW (both LYSO)	17.7	13.6	17.0	12.4	17.8	13.3	17.1	12.5

Table 5: FOW PSF.

	MPS AM	MPS PRED	MPS MC	KES AM	KES PRED	KES MC
Spatial resolution	$s(1+\frac{d_1}{D})$	14.52 mm	17.35 mm	$s_e(1+\frac{d_1}{d_2})$	13.5 mm	12.94 mm
Efficiency	$\frac{Hs}{4\pi LD}(1-f)$	$4.18 \cdot 10^5$	$2.22 \cdot 10^{-5}$	$\frac{Hs}{4\pi Ld_2}(1+x^2/d_2^2)^{-3/2}$	$6.67 \cdot 10^5$	$3.96 \cdot 10^{-5}$

Table 6: MPS and KES detection efficiencies and spatial resolution from analytical models. The predictions of the analytical model (AM column) are given in table **??**. The MC data is the average of the results for all selection criteria combinations. TODO: put in correct MC data, but first wait for decision on which selection to take.

Time selection	ToF				none			
Energy selection	1		3		1		3	
Camera	MPS	KES	MPS	KES	MPS	KES	MPS	KES
FRP (detectors as proposed)	–							
FRP (both LYSO absorber)	0.55	1.04	0.70	1.51	0.94	1.97	1.40	5.51

Table 7: Fall-off retrieval precision (defined as the standard deviation of the FOP over the number of times the simulation is ran.

The results are a bit worse than the calculated values in table **??**, but close to the 20 mm as postulated in Priegnitz et al. (2015).

When we make the collimator perfectly absorbing (we kill any tracks entering the material), we can see the KES's effective slit width in action: the transmission through the collimator creating a wider s_e is gone and we see the FOW decrease between 40 and 100%. This is roughly in line with the calculated s_e: ETIENNE? Surprisingly the FOW of the KES approaches the theoretical value nearly, while the MPS is still a few millimeters worse than calculated.

- Formulas of the the MPS and KES detection efficiencies and spatial resolution from analytical models (figure **??**)
  - Draw some conclusions about the intrinsic features of MPS and KES collimators knowing that the falloff retrieval precision (FRP)
    * Efficiency: same efficiency with the same $s, L, H, d_2(\text{KES}) = D(\text{MPS}), d_2(\text{MPS}) = 0$ (no space between collimator and absorber in MPS) and $f \longrightarrow 0$ (perfect collimator). In practice, $f \neq 0$ ($f = 0.4$ in the CLaRyS MPS camera) so that the KES camera has a slightly larger efficiency than the MPS camera with the aforementioned geometrical conditions. It is worth noting that the KES detection efficiency is not constant over the FOV.
    * Spatial resolution: same resolution with the same geometrical conditions and perfect collimators. In practice, MPS transparency can be neglected in the CLaRyS prototype ($D = 180$ mm) but not the KES transparency so that the KES camera has a slightly poorer spatial resolution than the one of the MPS camera (still with the aforementioned geometrical conditions).
  - Estimate the MPS and KES performances in Smeets 2016 and Lin 2017: the KES/MPS detection efficiency ratio is 1.6 for Smeets 2016 and 5.3 for Lin 2017 (assuming the use of the same energy window) $\Rightarrow$ these comparisons were unfair. . .

Smeets 2016

	Geometrical calculations	
	MPS	KES
d1 (mm)	300	300
D (mm)	200	
d2 (mm)	300	300
L (mm)	800	600
s (mm)	2	6
septa (mm)	2	
f	0,5	
Effective thickness (mm)	100	40
Det. Unit FOV (mm)	5	12
Lin. Coll. Eff (relative)	6,25E-006	3,33E-005
Falloff amplitude (4 mm bin)		
KES eff/ MPS eff	5,3333333333	

* no KES transparency taken into account
** Efficiency at the center of the camera

(a) Smeets 2016 setup   (b) Lin's setup

Figure 3: MPS and KES comparisons in litterature.

(Roellinghoff et al. (2014) shows impact of TOF)

I think it would be better to show PG profiles with 1-8 MeV energy selection with no TOF selection. The advantage of these selections is that it allows us to show the impact of energy ($>$1 MeV vs 3-6 MeV selection for KES) and TOF selection (for MPS) when we move to the prototypes configurations. We can put in the table of Figure 5 the result with the 3-6 MeV energy selection to show that the results do not depend on energy selection).
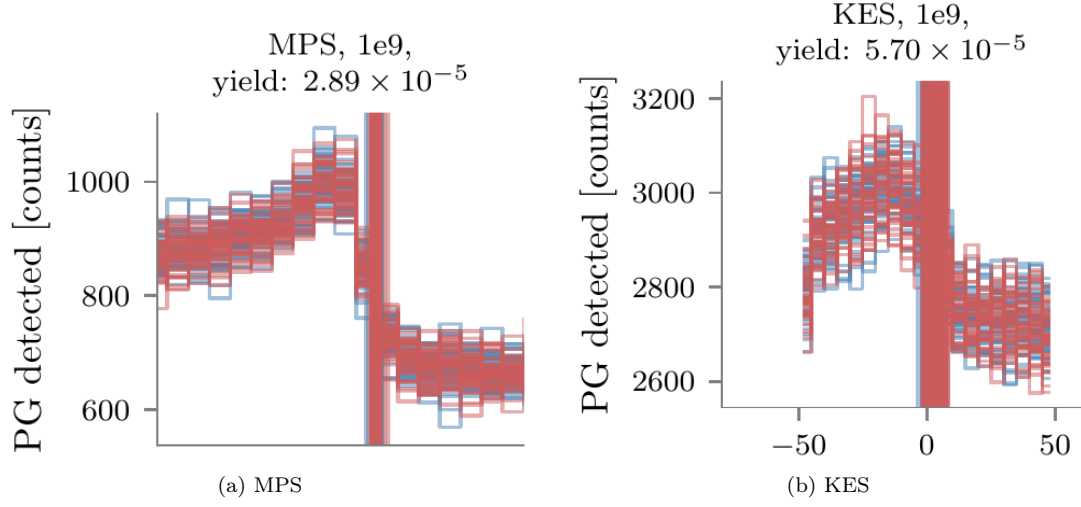
Figures 4 and 5.

(a) MPS

(b) KES

Figure 4: MPS and KES comparisons with the same absorber and the same energy (3-6 MeV) and TOF selection (no TOF selection). Sum the statistics of the various 1e9 PG profiles to get the smoothest profiles (we are interested in PG profile shapes). This will allow us to better estimate the falloff features, namely amplitude and width. Put the 2 PG profiles on a single figure?

| | MPS | KES | | | Simulation results | | | |
| | | | | NoTOF 3-6 MeV | | TOF 1-8 MeV | |
	MPS	KES		MPS	KES	MPS	KES
d1 (mm)	304	250					
D (mm)	180						
d2 (mm)	0	200					
L (mm)	484	450					
s (mm)	5.4	6*					
septa (mm)							
f	0.325						
Effective thickness (mm)	58.5	40		72			
Det. Unit FOV (mm)	14.52	13.5					
Lin. Coll. Eff (relative)	4.18E-005	6.67E-005**					
Falloff amplitude (4 mm bin)				200	350	400	700
KES eff/ MPS eff	1.59341564			1.75		1.75	
* no KES transparency taken into account							
** Efficiency at the center of the camera							

Figure 5: MPS and KES comparisons with the same absorber, energy and TOF selection. The first columns of the table correspond to the geometrical calculations. It is interesting to show the results for the two energy selections but it would be nice to have only one TOF selection (no TOF).

3.2 Prototype Comparison

Performance under clinical conditions is the eventual purpose of these PG cameras, and therefore we here include the results of the clinical case study. Since both cameras prototypes were optimized assuming their particular choice for absorber and energy selection window, here we chose to set
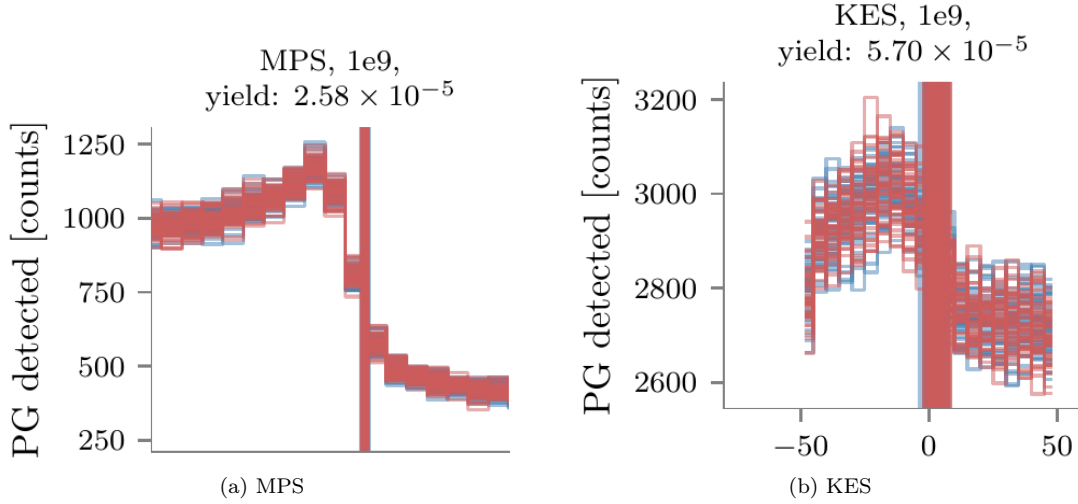
3.2.1 PG profiles

Figure 6.

(a) MPS

(b) KES

Figure 6: MPS and KES prototypes comparisons. MPS BGO aborber with 1-8 MeV energy selection and TOF selection. KES: LYSO absorber with 3-6 MeV and no TOF selection). Sum the statistics of the various 1e9 PG profiles to get the smoothest profiles (we are interested in PG profile shapes). This will allow us to better estimate the falloff features, namely amplitude and width. Put the 2 PG profiles on a single figure?

KES/MPS ratio $\sim 400/350 \sim 0.9$.

3.2.2 FRP

Figure showing the falloff retrieval precision (FRP) (standard deviation of the falloff position distributions) for the 2 prototypes as a function of the number of incident protons (10^7, 10^8, 10^9).

We do not have this figure yet. The figure in the spot grouping paper shows the mean and standard deviations on the falloff position differences for the 3 spots considered.

4 Discussion

5 Conclusion

6 Acknowledgements

A Fall-off position and width estimation procedure

A.1 Fall-off position estimation procedure

From a clinical perspective, the range estimate could be more interesting than FOP, because it can distinguish simple offset errors from patient morphological change. While the MPS camera was conceived for whole range PG profile detection, the KES camera FoV was chosen for BP region PG detection only. To make the comparison fair, only the FOP could be considered. Multiple approaches to extracting a FOP from the line profile have been proposed (Gueth et al., 2013; Janssen et al., 2014; Roellinghoff et al., 2014; Smeets et al., 2012; Sterpin et al., 2015). In preparatory work, a number of the proposed procedures were investigated. Significant sensitivity to free parameters on the final FOP estimates were seen. In summary, the FOP estimate depends greatly on the procedure, and often on having yields uncommon on the spot-level in clinical TPs, and also on an absence of unavoidable inhomogeneities.

Therefore the fitting method was not chosen as a topic for study in this paper. Instead, a simple method that works on most the data available to the authors was used: first a smoothed and interpolated spline function is fitted against the detected PG data points, after which a baseline and (distal) peak position are determined. The intersection of the spline with the half-height of the peak above the baseline is then taken as the FOP. A more detailed description of the procedure may be found in appendix A.

1. The measured PG profile is smoothed and interpolated with a smoothing spline function:

$$\sum_{i=1}^{n}(y_i - \hat{f}(x_i))^2 + \lambda \int_{x_1}^{x_n} \hat{f}''(x)^2 \, dx \tag{9}$$

   where y_i is the measured PG profile and x_i the associated x-coordinates, $\hat{f}(x_i)$ the estimate smoothed spline function and λ a smoothing parameter that determines the penalty for deviating from measurement in exchange for smoothness (second order derivatives are close to zero on smooth functions). $\lambda = 0$ produces a perfect spline fit to the data, while $\lambda \gg 1$ produces a horizontal line. We found that $\lambda = 2$ provided an acceptable trade-off between overfitting to noise and removing too many features, which tends to happen for low statistic measurements.

2. The obtained function is plotted for 1024 x_j, an number that provided a sufficiently high resolution. Any $f(x_j) < 0$ are set to 0.

3. The global maximum is found.

4. The baseline is set equal to the lowest 25% of bins.

5. From the distal end backwards, the first maximum is taken as the distal most peak position, if it is above the threshold of 30% of the difference between baseline and global maximum. If no such point is found, the global maximum is taken as the distal most maximum.

6. The fall-off amplitude (FOA) is set to the difference between the distal maximum and baseline: $FOA = max - baseline$. The FOP is obtained by traversing the smoothed profile from the distal end towards the peak until $y_j > \frac{1}{2}FOA$.

The results of this procedure are illustrated in figure 7. Every PG profile was estimated 50 times, and so we obtained 50 estimates for the FOP. It is assumed that the FOPs follow a Gaussian distribution, so the mean of the 50 realizations gives the best FOP estimate and the sigma gives the precision of the ability to estimate the best FOP. Comparing the 50 FOP estimates obtained from the CT with the 50 estimates obtained from the RPCT simulations, gives 2500 possible shift estimates. Again, the distribution of shifts should be centered at the true shift, while the sigma indicates how likely it is that this true shift is detected under the current conditions.

A.2 Fall-off width estimation procedure

Figure 8 shows and illustration of the procedure for two selected profiles obtained with each collimator. To estimate the fall-off with FOW, we smooth the profile in a similar manner as for the FOP estimation, as detailed in appendix A (row 1 in fig. 8). Then, a first and second order derivative is computed. On the first order derivative, a Gaussian is fitted (dashed line on second row), on the interval (solid line) between the profile maximum (Bragg Peak) and the first inflection point past the FOP on the second order derivative (here the 1D PG profile is at the baseline of the background, see third row). The
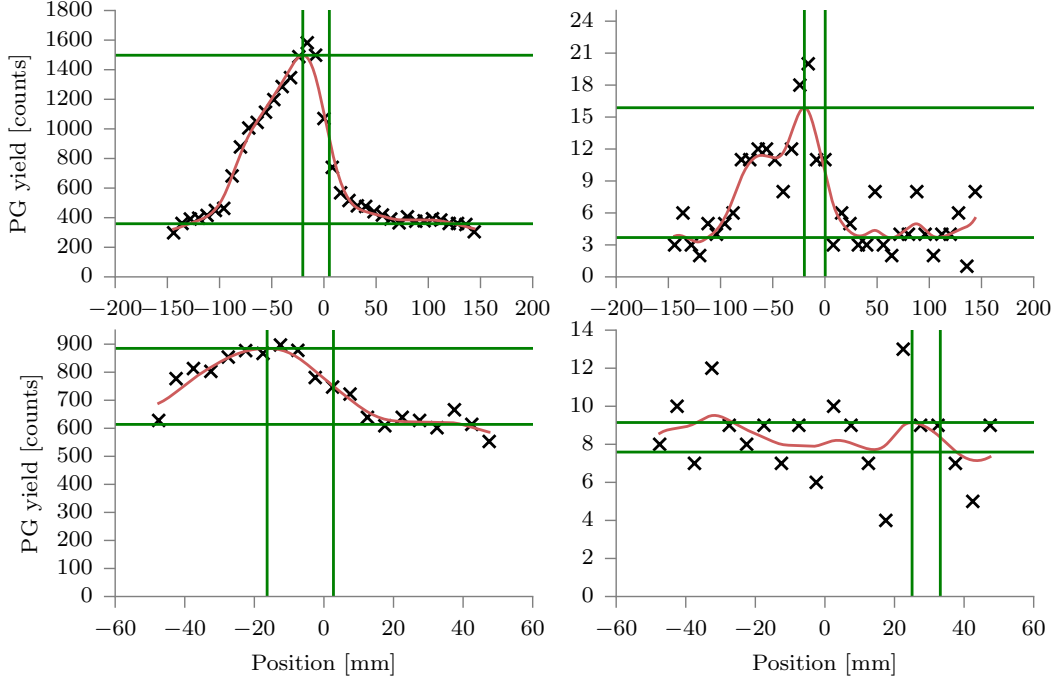
Figure 7: The top row demonstrates the fall-off determination procedure on the multi-parallel camera data; on the bottom row on knife-edge slit camera data. The left column is produced with a PG signal due to 10^9 primaries, while the right column was produced with 10^7 primary protons. In black crosses the measured PG counts are plotted. The smoothed data is shown in red. The green horizontal lines are drawn at the obtained distal maxima and baselines, while the vertical green lines shown the position of the distal maximum and the position of the fall-off. For the bottom-right plot, a history is visible where the procedure fails: the background induces an erroneous peak detection.
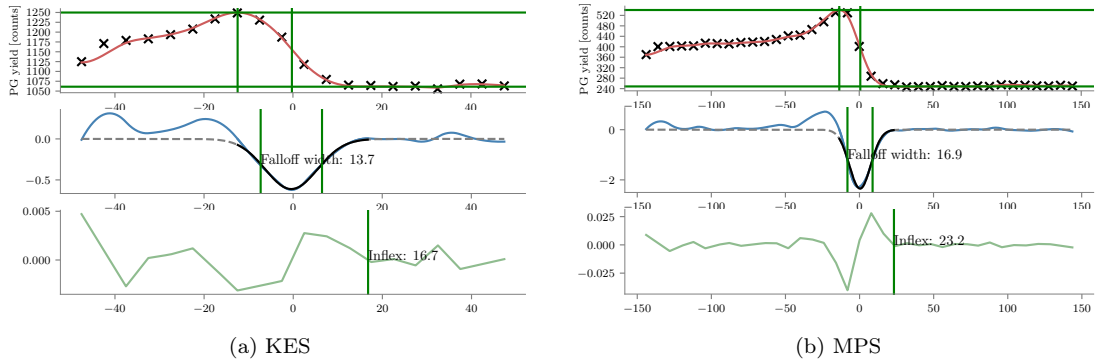

(a) KES

(b) MPS

Figure 8: MPS and KES FOW estimation illustrated.

Gaussian is fit with a fixed offset of zero, because the baseline of the background is zero. The full width half max of the fitted Gaussian is then taken as the FOW (second row).

B   Verification of the cameras

In Priegnitz et al. (2015) PG shifts due to beam energy shifts are studied for the KES camera: the *detectability* of the fall-off as function of the number of primaries. Here that simulation was recreated: a mono-energetic beam shoots into a waterbox at two energies. 50 realizations are generated with a 139 MeV beam energy, and 50 realizations with 144 MeV. At 10^9 primaries, the distributions are well separated with a shift of 8.3 mm (different from Priegnitz et al. (2015) because of the different material). In figure 13 in Perali et al. (2014) with 10^9 primaries a standard deviation of 1.5 mm is obtained, while here 1.21 and 1.14 mm were obtained. It is sufficient agreement to be confident of our setup and further results.

The KES prototype's sensitivity to accurate positioning with respect to the expected FOP was elaborated upon in Sterpin et al. (2015, Section IV.A.3): the detector response is, due to the KES collimator, not linear as with a parallel slit collimator. In this study, to make the comparison as fair as possible and avoid any bias, alignment on the FOP specific for each spot was ensured as follows: the intermediate PG source image of vpgTLE (equivalent to the PG emission) was projected on the beam axis, and then convolved with a Gaussian of $\sigma = 8.5$ mm, which corresponds to the point spread function (PSF) with a FWHM of 20 mm used in Priegnitz et al. (2015) to approximate the detected profiles from the emitted profile. These profiles will be referred to as "PG + PSF" profiles. As a matter of fact, the MPS prototype has roughly the same PSF as the KES prototype so that "PG + PSF" fall-off position can be considered as the expected position for both cameras.

To verify the implementation of the MPS camera, the precision on the FOP, obtained with the procedure outlined in the previous paragraph, is compared to earlier results. In the caption of figure 9 in Pinto et al. (2014) it is stated that with 10^8 primaries a standard deviation of 1.3 mm is obtained for the detector design used here, which is about 20% different from the results obtained in this study: 1.63 and 1.54 mm.

References

Christian Golnik, Fernando Hueso-González, Andreas Müller, Peter Dendooven, Wolfgang Enghardt, Fine Fiedler, Thomas Kormoll, Katja Roemer, Johannes Petzoldt, Andreas Wagner, and Guntram Pausch. Range assessment in particle therapy based on prompt γ-ray timing measurements. *Physics in Medicine and Biology*, 59(18):5399–5422, sep 2014. ISSN 0031-9155. doi: 10.1088/0031-9155/59/18/5399. URL http://stacks.iop.org/0031-9155/59/i=18/a=5399?key=crossref.5437fcd3059992135ec2113679c7dad6.

P Gueth, D Dauvergne, N Freud, J M Létang, C Ray, E Testa, and D Sarrut. Machine learning-based patient specific prompt-gamma dose monitoring in proton therapy. *Physics in medicine and biology*, 58(13):4563–77, jul 2013. ISSN 1361-6560. doi: 10.1088/0031-9155/58/13/4563. URL http://www.ncbi.nlm.nih.gov/pubmed/23771015.

Brent F B Huisman, J M Létang, É Testa, and D Sarrut. Accelerated Prompt Gamma estimation for clinical Proton Therapy simulations. *Physics in Medicine and Biology*, 61:7725–7743, 2016. ISSN 0031-9155. doi: 10.1088/0031-9155/61/21/7725.

F M F C Janssen, G Landry, P Cambraia Lopes, G Dedes, J Smeets, D R Schaart, K Parodi, and F Verhaegen. Factors influencing the accuracy of beam range estimation in proton therapy using prompt gamma emission. *Physics in medicine and biology*, 59(15):4427–41, aug 2014. ISSN 1361-6560. doi: 10.1088/0031-9155/59/15/4427. URL http://www.ncbi.nlm.nih.gov/pubmed/25049223.

Antje-Christin Knopf and Antony Lomax. In vivo proton range verification: a review. *Physics in medicine and biology*, 58(15):R131–60, aug 2013. ISSN 1361-6560. doi: 10.1088/0031-9155/58/15/R131. URL http://www.ncbi.nlm.nih.gov/pubmed/23863203.

J. Krimmer, D. Dauvergne, J.M. Létang, and É. Testa. Prompt-gamma monitoring in hadrontherapy: A review. *Nuclear Instruments and Methods in Physics Research Section A: Accelerators, Spectrometers, Detectors and Associated Equipment*, aug 2017. ISSN 01689002. doi: 10.1016/j.nima.2017.07.063. URL http://linkinghub.elsevier.com/retrieve/pii/S0168900217308380.

Shunsuke Kurosawa, Hidetoshi Kubo, Kazuki Ueno, Shigeto Kabuki, Satoru Iwaki, Michiaki Takahashi, Kojiro Taniue, Naoki Higashi, Kentaro Miuchi, Toru Tanimori, Dogyun Kim, and Jongwon Kim. Prompt gamma detection for range verification in proton therapy. *Current Applied Physics*, 12(2): 364–368, 2012. ISSN 15671739. doi: 10.1016/j.cap.2011.07.027. URL http://dx.doi.org/10.1016/j.cap.2011.07.027.

Yi-Chun Lin, C.Y. Pan, K.J. Chiang, M.C. Yuan, C.H. Chu, Y.W. Tsai, P.K. Teng, C.H. Lin, T.C. Chao, C.C. Lee, C.J. Tung, and A.E. Chen. Monte carlo simulations for angular and spatial distributions in therapeutic-energy proton beams. *Radiation Physics and Chemistry*, 140:217 – 224, 2017. ISSN 0969-806X. doi: https://doi.org/10.1016/j.radphyschem.2017.03.018. URL http://www.sciencedirect.com/science/article/pii/S0969806X17302980. 2nd International Conference on Dosimetry and its Applications (ICDA-2) University of Surrey, Guildford, United Kingdom, 3-8 July 2016.

Gabriela Llosá, Marco Trovato, John Barrio, Ane Etxebeste, Enrique Muñoz, Carlos Lacasta, Josep F. Oliver, Magdalena Rafecas, Carles Solaz, and Paola Solevi. First Images of a Three-Layer Compton Telescope Prototype for Treatment Monitoring in Hadron Therapy. *Frontiers in Oncology*, 6(February): 14, 2016. ISSN 2234-943X. doi: 10.3389/fonc.2016.00014. URL http://journal.frontiersin.org/Article/10.3389/fonc.2016.00014/abstract.

S D Metzler and R Accorsi. Resolution- versus sensitivity-effective diameter in pinhole collimation: experimental verification. *Physics in Medicine and Biology*, 50(21):5005–5017, nov 2005. ISSN 0031-9155. doi: 10.1088/0031-9155/50/21/004. URL http://www.ncbi.nlm.nih.gov/pubmed/16237237http://stacks.iop.org/0031-9155/50/i=21/a=004?key=crossref.554d8443522872c9a60e734710db9839.

M Moteabbed, S España, and H Paganetti. Monte Carlo patient study on the comparison of prompt gamma and PET imaging for range verification in proton therapy. *Physics in medicine and biology*, 56

(4):1063–82, feb 2011. ISSN 1361-6560. doi: 10.1088/0031-9155/56/4/012. URL http://www.ncbi.nlm.nih.gov/pubmed/21263174.

Harald Paganetti. Range uncertainties in proton therapy and the role of Monte Carlo simulations. *Physics in Medicine and Biology*, 57(11):R99–R117, 2012. ISSN 0031-9155. doi: 10.1088/0031-9155/57/11/R99. URL http://stacks.iop.org/0031-9155/57/i=11/a=R99?key=crossref.4b6c83cb5125b4a360ead936994fceb4.

I Perali, a Celani, L Bombelli, C Fiorini, F Camera, E Clementel, S Henrotin, G Janssens, D Prieels, F Roellinghoff, J Smeets, F Stichelbaut, and F Vander Stappen. Prompt gamma imaging of proton pencil beams at clinical dose rate. *Physics in Medicine and Biology*, 59(19):5849–5871, oct 2014. ISSN 0031-9155. doi: 10.1088/0031-9155/59/19/5849. URL http://stacks.iop.org/0031-9155/59/i=19/a=5849?key=crossref.d1c598721e0b970b36f1c8a6ad1dd1a1.

M Pinto, D Dauvergne, N Freud, J Krimmer, J M Letang, C Ray, F Roellinghoff, and E Testa. Design optimisation of a TOF-based collimated camera prototype for online hadrontherapy monitoring. *Physics in medicine and biology*, 59(24):7653–7674, 2014. ISSN 1361-6560. doi: 10.1088/0031-9155/59/24/7653. URL http://www.ncbi.nlm.nih.gov/pubmed/25415207.

Jerimy C Polf, Stephen Avery, Dennis S Mackin, and Sam Beddar. Imaging of prompt gamma rays emitted during delivery of clinical proton beams with a Compton camera: feasibility studies for range verification. *Phys Med Biol*, 60(18):7085–7099, 2015. ISSN 0031-9155. doi: 10.1088/0031-9155/60/18/7085. URL http://dx.doi.org/10.1088/0031-9155/60/18/7085.

M Priegnitz, S Helmbrecht, G Janssens, and I Perali. Measurement of prompt gamma profiles in inhomogeneous targets with a slit camera. *Physics in Medicine and Biology*, 4849:4849, 2015. ISSN 0031-9155. doi: 10.1088/0031-9155/60/12/4849. URL http://dx.doi.org/10.1088/0031-9155/60/12/4849.

Christian Richter, Guntram Pausch, Steffen Barczyk, Marlen Priegnitz, Isabell Keitz, Julia Thiele, Julien Smeets, Francois Vander Stappen, Luca Bombelli, Carlo Fiorini, Lucian Hotoiu, Irene Perali, Damien Prieels, Wolfgang Enghardt, and Michael Baumann. First clinical application of a prompt gamma based in vivo proton range verification system. *Radiotherapy and Oncology*, 118(2):232–237, 2016. ISSN 18790887. doi: 10.1016/j.radonc.2016.01.004. URL http://linkinghub.elsevier.com/retrieve/pii/S0167814016000074.

C Robert, G Dedes, G Battistoni, T T Böhlen, I Buvat, F Cerutti, M P W Chin, a Ferrari, P Gueth, C Kurz, L Lestand, a Mairani, G Montarou, R Nicolini, P G Ortega, K Parodi, Y Prezado, P R Sala, D Sarrut, and E Testa. Distributions of secondary particles in proton and carbon-ion therapy: a comparison between GATE/Geant4 and FLUKA Monte Carlo codes. *Physics in medicine and biology*, 58(9):2879–99, may 2013. ISSN 1361-6560. doi: 10.1088/0031-9155/58/9/2879. URL http://www.ncbi.nlm.nih.gov/pubmed/23571094.

F. Roellinghoff, M. H. Richard, M. Chevallier, J. Constanzo, D. Dauvergne, N. Freud, P. Henriquet, F. Le Foulher, J. M. Létang, G. Montarou, C. Ray, E. Testa, M. Testa, and a. H. Walenta. Design of a Compton camera for 3D prompt-γ imaging during ion beam therapy. *Nuclear Instruments and Methods in Physics Research, Section A: Accelerators, Spectrometers, Detectors and Associated Equipment*, 648(SUPPL. 1):S20–S23, aug 2011. ISSN 01689002. doi: 10.1016/j.nima.2011.01.069. URL http://linkinghub.elsevier.com/retrieve/pii/S0168900211001471.

F Roellinghoff, a Benilov, D Dauvergne, G Dedes, N Freud, G Janssens, J Krimmer, J M Létang, M Pinto, D Prieels, C Ray, J Smeets, F Stichelbaut, and E Testa. Real-time proton beam range monitoring by means of prompt-gamma detection with a collimated camera. *Physics in medicine and biology*, 59(5):1327–38, 2014. ISSN 1361-6560. doi: 10.1088/0031-9155/59/5/1327. URL http://www.ncbi.nlm.nih.gov/pubmed/24556873.

David Sarrut, Manuel Bardiès, Nicolas Boussion, Nicolas Freud, Sébastien Jan, Jean-Michel Létang, George Loudos, Lydia Maigne, Sara Marcatili, Thibault Mauxion, Panagiotis Papadimitroulas, Yann Perrot, Uwe Pietrzyk, Charlotte Robert, Dennis R Schaart, Dimitris Visvikis, and Irène Buvat. A review of the use and potential of the GATE Monte Carlo simulation code for radiation therapy and

dosimetry applications. *Medical Physics*, 41(6), 2014. doi: http://dx.doi.org/10.1118/1.4871617. URL http://scitation.aip.org/content/aapm/journal/medphys/41/6/10.1118/1.4871617.

J Smeets, F Roellinghoff, D Prieels, F Stichelbaut, A Benilov, P Busca, C Fiorini, R Peloso, M Basilavecchia, T Frizzi, J C Dehaes, and A Dubus. Prompt gamma imaging with a slit camera for real-time range control in proton therapy. *Physics in medicine and biology*, 57(11):3371–405, 2012. ISSN 1361-6560. doi: 10.1088/0031-9155/57/11/3371. URL http://www.ncbi.nlm.nih.gov/pubmed/22572603.

Julien Smeets, Frauke Roellinghoff, Guillaume Janssens, Irene Perali, Andrea Celani, Carlo Fiorini, Nicolas Freud, Etienne Testa, and Damien Prieels. Experimental comparison of knife-edge and multi-parallel slit collimators for prompt gamma imaging of proton pencil beams. *Frontiers in Oncology*, 6: 156, 2016. ISSN 2234-943X. doi: 10.3389/fonc.2016.00156. URL https://www.frontiersin.org/article/10.3389/fonc.2016.00156.

Paola Solevi, Enrique Muñoz, Carles Solaz, Marco Trovato, Peter Dendooven, John E Gillam, Carlos Lacasta, Josep F Oliver, Magdalena Rafecas, Irene Torres-Espallardo, Gabriela Llosá, Agostinelli S et Al, Solaz C Barrio J, Etxebeste A, Lacasta C, Muñoz E, Oliver J, Llosá G, Llosá G Cabello J, Etxebeste A, Ziegler S I, Enghardt W et Al, Barrio J Gillam J E, Lacasta C, Torres-Espallardo I, Candela Juan C, Llosá G, Solevi P, Rafecas M, Golnik C et Al, Jan S et Al, Ivanov P Klöckner A, Pinto N, Lee Y, Catanzaro B, Fasih A, Knopf A A, Lomax, Zuber K Kormoll T, Fiedler F, Schóne S, Wüstemann J, Enghardt W, Bruyndonckx P Li Z, Wedrowski M, Vandersteen G, Solaz C Llosá G, Trovato M, Barrio J, Etxebeste A, Munoz E, Lacasta C, Oliver J F, Rafecas M, Solevi P, Llosá G et Al, Llosá G et Al, Thomas D J Marsh J W, Burke M, Meier D et Al, Youn M Y Min C H, Kim C H, Kim J W, Ortega P G et Al, Robertson D Peterson S W, Polf J, Pinto M et Al, Roellinghoff F Pinto M, Dauvergne D, Freud N, Krimmer J, Letang J M, Ray C, Testa E, Mackin D S Polf J C, Avery S, Beddar S, Polf J C et Al, Robert C et Al, Schumann A Rohling H, Golnik C, Enghardt W, Hueso-González F, Kormoll T, Pausch G, Fiedler F, Elsässer T Schardt D, Schulz-Ertner D, Roemer K Schumann A, Petzoldt J, Dendooven P, Enghardt W, Golnik C, Hueso-González F, Kormoll T, Pausch G, Fiedler F, Priegnitz M Shakirin G, Braess H, Fiedler F, Kunath D, Laube K, Parodi K, Enghardt W, Smeets J et Al, Trovato M Stankova V, Barrio J, Gillam J E, Lacasta C, Rafecas M, Solaz C, Llosá G, Bortfeld T Verburg J M, Riley K, Seco J, Xu D Z, and He. Performance of MACACO Compton telescope for ion-beam therapy monitoring: first test with proton beams. *Physics in Medicine and Biology*, 61(14): 5149–5165, 2016. ISSN 0031-9155. doi: 10.1088/0031-9155/61/14/5149. URL http://stacks.iop.org/0031-9155/61/i=14/a=5149?key=crossref.6bf836448c34a4bc8348edeba28d35c4.

E Sterpin, G Janssens, J Smeets, François Vander Stappen, D Prieels, Marlen Priegnitz, Irene Perali, and S Vynckier. Analytical computation of prompt gamma ray emission and detection for proton range verification. *Physics in Medicine and Biology*, 60(12):4915–4946, 2015. ISSN 0031-9155. doi: 10.1088/0031-9155/60/12/4915. URL http://stacks.iop.org/0031-9155/60/i=12/a=4915?key=crossref.aabd8815e135401a22d165e343a7bac4.

E. Testa, M. Bajard, M. Chevallier, D. Dauvergne, F. Le Foulher, N. Freud, J. M. Letang, J. C. Poizat, C. Ray, and M. Testa. Monitoring the Bragg peak location of 73 MeVu carbon ions by means of prompt ?? -ray measurements. *Applied Physics Letters*, 93(9):1–10, 2008. ISSN 00036951. doi: 10.1063/1.2975841. URL http://arxiv.org/abs/0809.0185http://dx.doi.org/10.1063/1.2975841.

P.G. Thirolf, S. Aldawood, M. Böhmer, J. Bortfeldt, I. Castelhano, G. Dedes, F. Fiedler, R. Gernhäuser, C. Golnik, S. Helmbrecht, F. Hueso-González, H. v.d. Kolff, T. Kormoll, C. Lang, S. Liprandi, R. Lutter, T. Marinšek, L. Maier, G. Pausch, J. Petzoldt, K. Römer, D. Schaart, and K. Parodi. A Compton camera prototype for prompt gamma medical imaging. *EPJ Web of Conferences*, 117:05005, 2016. ISSN 2100-014X. doi: 10.1051/epjconf/201611705005. URL http://www.epj-conferences.org/10.1051/epjconf/201611705005.

Joost M Verburg and Joao Seco. Proton range verification through prompt gamma-ray spectroscopy. *Physics in Medicine and Biology*, 59(23):7089–7106, 2014. ISSN 0031-9155. doi: 10.1088/0031-9155/59/23/7089. URL http://stacks.iop.org/0031-9155/59/i=23/a=7089?key=crossref.2c380dcfa8360cb6e6defe62dd49f24a.